

Hot Deformation Behavior of Novel Al-Cu-Y(Er)-Mg-Mn-Zr Alloys

Maxim G. Khomutov ¹, Sayed M. Amer ^{1,2}, Ruslan Yu. Barkov ^{1,*}, Maria V. Glavatskikh ¹, Alexander Yu. Churyumov ¹ and Andrey V. Pozdniakov ¹

¹ Department of Physical Metallurgy of Non-Ferrous Metals, National University of Science and Technology “MISIS”, Leninskiy Prospekt 4, 119991 Moscow, Russia; khomutov@isis.ru (M.G.K.); e.khames@isis.ru (S.M.A.); mariaglavatskih@yandex.ru (M.V.G.); Churyumov@isis.ru (A.Y.C.); pozdniakov@isis.ru (A.V.P.)

² Metallurgy and Petroleum Engineering Department, Faculty of Engineering, Al-Azhar University, Cairo 11884, Egypt

* Correspondence: barkov@isis.ru

Abstract: The compression tests in a temperature range of 400–540 °C and strain rates of 0.1–15 s^{−1} were applied to novel Al-Cu-Y(Er)-Mg-Mn-Zr alloys to investigate their hot deformation behavior. The higher volume fraction of the intermetallic particles with a size of 0.5–4 μm in the alloys caused an increase in flow stress. Hyperbolic sine law constitutive models were constructed for the hot deformation behavior of Al-Cu-Y(Er)-Mg-Mn-Zr alloys. Effective activation energy has a higher value in the alloys with Er than in the alloys with Y. According to the processing maps, the temperature range of 420–480 °C and strain rates higher than 5 s^{−1} are the most unfavorable region for hot deformation for the investigated alloys. The deformation at 440 °C and 15 s^{−1} led to cracks on the surface of the sample. However, internal cracks were not observed in the microstructure after deformation. The optimum hot deformation temperatures were in a range of 500–540 °C and at strain rates of 0.1–15 s^{−1}.

Keywords: aluminum alloys; erbium; yttrium; hot deformation behavior; constitutive modeling; processing maps



Citation: Khomutov, M.G.; Amer, S.M.; Barkov, R.Y.; Glavatskikh, M.V.; Churyumov, A.Y.; Pozdniakov, A.V. Hot Deformation Behavior of Novel Al-Cu-Y(Er)-Mg-Mn-Zr Alloys. *Metals* **2021**, *11*, 1521. <https://doi.org/10.3390/met11101521>

Academic Editors: Daolun Chen and Maciej Motyka

Received: 25 August 2021
Accepted: 22 September 2021
Published: 24 September 2021

Publisher’s Note: MDPI stays neutral with regard to jurisdictional claims in published maps and institutional affiliations.



Copyright: © 2021 by the authors. Licensee MDPI, Basel, Switzerland. This article is an open access article distributed under the terms and conditions of the Creative Commons Attribution (CC BY) license (<https://creativecommons.org/licenses/by/4.0/>).

1. Introduction

Aluminum alloys play a significant role in the industry due to their high specific strength, corrosion-resistance, and workability during casting and deformation processing. Such two processes are the main stages of aluminum alloy production and heat treatment, which form the microstructure of the products. Hot deformation behavior plays an important role in investigations and the development of novel aluminum alloys [1–7]. Hot deformation can significantly improve the microstructure of as-cast materials due to decreasing the porosity, the size of the crystallization origin particles, and the grain size. It considerably enhances the strength and plasticity of materials.

Novel Al-Cu-Y [8–12] and Al-Cu-Er [9,13–16] alloys demonstrate enhanced casting and mechanical properties due to a wide solidification range [8,9,11,17–20] and particle dispersion and thermally stable structure [8–16]. Perspective quasibinary Al-Cu-Ce alloys also exhibit such properties [21]. Multicomponent alloys [12,16] demonstrate high hardness and tensile strength after heat and thermomechanical treatments due to the formation of nano-sized precipitates under solution treatment and aging. The formation of micron-sized intermetallic particles of solidification origin provide high yield strength at elevated temperatures [22,23].

The development of the optimal technology of hot deformation requires the response of the material under different thermomechanical conditions. Usually, thermomechanical simulators are used for the determination of rheological properties [24,25]. However, the true stress–true strain curves are obtained only in discrete mode for a limited set of strain rates and temperatures. The constitutive modeling of hot deformation behavior

is required to extend the mechanical testing results on continuous ranges of strain rates and temperatures [26]. Recently, constitutive models were constructed for a wide range of aluminum alloys such as 2A14 [26], AA6099 [27], and AA6061 [28]. Most of the publications have been devoted to investigating alloys with a small number of eutectic origin particles. However, it is known that such particles may significantly influence hot deformation behavior [29–33]. For example, it was found that the flow stress was lowered by decreasing the Al₃Ni size at a low 0.03 volume fraction in binary Al-Ni alloys and intensive softening at large strains was achieved in the alloy with a 0.1 volume fraction of fine Al₃Ni particles [29]. Wu et al. demonstrated the effect of micro-sized Si particles on the hot deformation behavior of Al-Si-Mg alloys [30]. This effect corresponds to particle-stimulated nucleation [30]. Mikhaylovskaya et al. showed that particle-stimulated nucleation occurred due to Al₃FeNi and Mg₂Si eutectic origin phases during hot tension of the Al-Mg-Si alloy doped with eutectic-forming Ni and Fe [31]. Zhang et al. investigated the effect of Al₄Sr particles on hot deformation behavior. In particular, they used constitutive modeling, which improved the hot extrusion process of the Al-10Sr master alloy [32]. However, few works have been devoted to investigating the effect of the Y and Er content phases on the hot deformation behavior of Al-Cu alloys. Chankitmongkol et al. showed that the AA4032 alloy with 3.5Cu and 0.4Er had a lower activation energy of deformation compared to the base alloy without Er [33]. The alloy with Er demonstrated more polygonized grains at a low strain rate than the alloys without Er, indicating that Er hindered recrystallization development [33].

The main hot deformation parameters are temperature, strain rate, and strain. However, the initial microstructure is critical for deformation behavior and microstructure formation [1]. This work aimed to investigate the hot deformation behavior of novel Al-Cu-Y(Er)-Mg-Mn-Zr alloys with different initial microstructures.

2. Materials and Methods

The composition of the investigated alloys is shown in Table 1. The alloys were melted from pure Al (99.7Al, 0.15Fe, and 0.15Si), Mg (99.9%), Al-10Mn, Al-5Zr, Al-5Ti-1B, Al-8Er, and Al-10Y master alloys in a resistance furnace at 830 °C. Melt was poured into a water-cooling copper mold with an ingot size of 20 × 40 × 120 mm³. Before hot compression, the samples were homogenized at 575 °C for 3 h [22,23]. Mechanical testing at elevated temperatures was carried out using a thermomechanical simulator Gleeble 3800 (Dynamic Systems Inc., Poestenkill, NY, USA). The samples for compression were cylinders with a height of 15 mm and a diameter of 10 mm. Hot compression proceeded in a temperature range of 400–540 °C and at strain rates of 0.1–15 s⁻¹. The heating of the samples to the hot compression temperature was carried out with the rate of 5 K/s. The soaking time before compression was 30 s. The samples were immediately quenched after the deformation by compressed air. The cooling rate was about of 20 K/s. The compression stress–strain curves were recalculated to consider friction and adiabatic heating during deformation [34,35]. Processing maps were constructed by B-spline interpolation using OriginLab Software (Version 9.1, Northampton, MA, USA).

Table 1. Composition of the investigated alloys.

Alloy	Cu	Er/Y	Mg	Mn	Zr	Fe	Si	Ti
AlCuYMg1	5.6	-/2	1	0.8	0.3	0.15	0.15	0.15
AlCuErMg1	5.4	3/-	1.1	0.9	0.3	0.15	0.15	0.15
AlCuYMg2	4.5	-/1.6	0.9	0.6	0.2	0.15	0.15	0.1
AlCuErMg2	4	2.7/-	0.8	0.8	0.2	0.15	0.15	0.1

The microstructure of the samples was investigated using a scanning electron microscope (SEM) Tescan-VEGA3 LMH (TESCAN, Brno, The Czech Republic) equipped with an energy dispersive X-ray spectrometer (EDS) (X-MAX80, Oxford Instruments Advanced AZtecEnergy, High Wycombe, UK) and a light microscope (LM) Carl Zeiss Axiovert 200

(Carl Zeiss AG, Oberkochen, Germany). The samples for the microstructural investigations were mechanically polished and electrochemically etched. The grain size, size, and volume fraction of intermetallic phase particles were determined by the linear intercept method.

3. Results and Discussion

3.1. Initial Microstructure

The initial grain structure and the phase composition of the alloys were investigated in detail in [22,23]. Figure 1 illustrates the typical microstructure of the AlCuErMg2 alloy in the as-homogenized state. The grain structure is shown in Figure 1a (LM) and the microstructure in the back scattered electron in Figure 1b (SEM). The dark phase is the aluminum solid solution (Al) and the light phases are the intermetallic particles. The average grain size of the AlCuYMg2 and AlCuErMg2 alloys was in the range of 80–100 μm (Figure 1a). A finer grain structure (25–40 μm) was seen in AlCuYMg1 and AlCuErMg1 due to higher Ti content [22]. The microstructure of the Al-Cu-Y and Al-Cu-Er system based quasibinary alloys with Zr, Mn, Ti, Mg addition was investigated in detail in previous works [8–16]. The aluminum solid solution (Al) and a fine eutectic ((Al)+Al₈Cu₄Y) and ((Al)+Al₈Cu₄Er) were the main structure parts of the Al-Cu-Y and Al-Cu-Er system based quasibinary alloys in the as-cast state. The low fraction of the AlCu, Al₃Er, (Al,Cu)₁₁Y₃ formed during solidification in the ternary alloys [8,9,13]. Manganese and magnesium additions led to formation of the Al₂₅Cu₄Mn₂Er, Al₂₅Cu₄Mn₂Y and Mg₂Si phases [12,16,22,23]. The non-equilibrium part of the intermetallic particles dissolved during homogenization treatment. Non-dissolving particles fragmented, spheroidized, and grew. As a result, the binary AlCu, Al₃Er, ternary Al₈Cu₄Y, (Al,Cu)₁₁Y₃, Al₈Cu₄Er, and quaternary Al₂₅Cu₄Mn₂Er, Al₂₅Cu₄Mn₂Y phases [8–16,22,23] with a size of 0.5–4 μm were present in the microstructure of the investigated alloys in the as-homogenized state. The average intermetallic phase particles size was $1.5 \pm 0.5 \mu\text{m}$. The volume fraction of the intermetallic particles for the alloys with elevated copper content AlCuYMg1 and AlCuErMg1 was in the range of 11–12% [22] and for the AlCuYMg2 and AlCuErMg2 alloys, it was 8.5% [23]. The microstructure parameters are presented in Table 2.

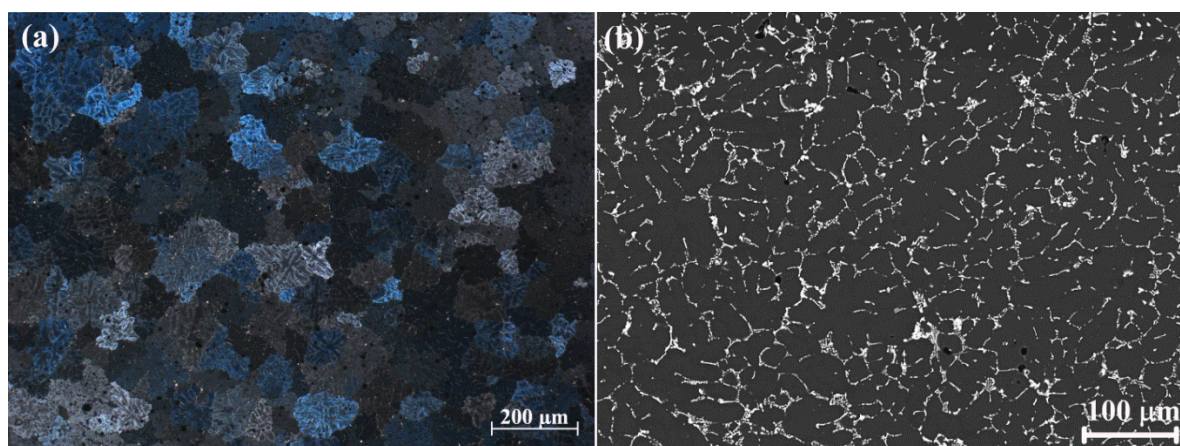


Figure 1. Microstructure of the AlCuErMg2 alloy in the as-homogenized state: (a) LM and (b) SEM.

Table 2. Microstructure parameters.

Alloy	Grain Size, μm	Intermetallic Particles Size, μm	Intermetallic Particles Volume Fraction, %
AlCuYMg1 and AlCuErMg1	25–40	0.5–4	11–12
AlCuYMg2 and AlCuErMg2	85–100	0.5–4	8.5

3.2. Hot Deformation Behavior

Typical stress–strain curves are shown in Figure 2. The stress increased with decreasing the compression temperature and increasing the strain rate for all the investigated alloys. The reasons for such behavior are as follows. The increase in temperature enhanced dislocation mobility, which accelerated the annihilation and rearrangement of dislocations. The increase in strain rate can offer stronger dislocation–dislocation interaction and a shorter time for dynamic softening.

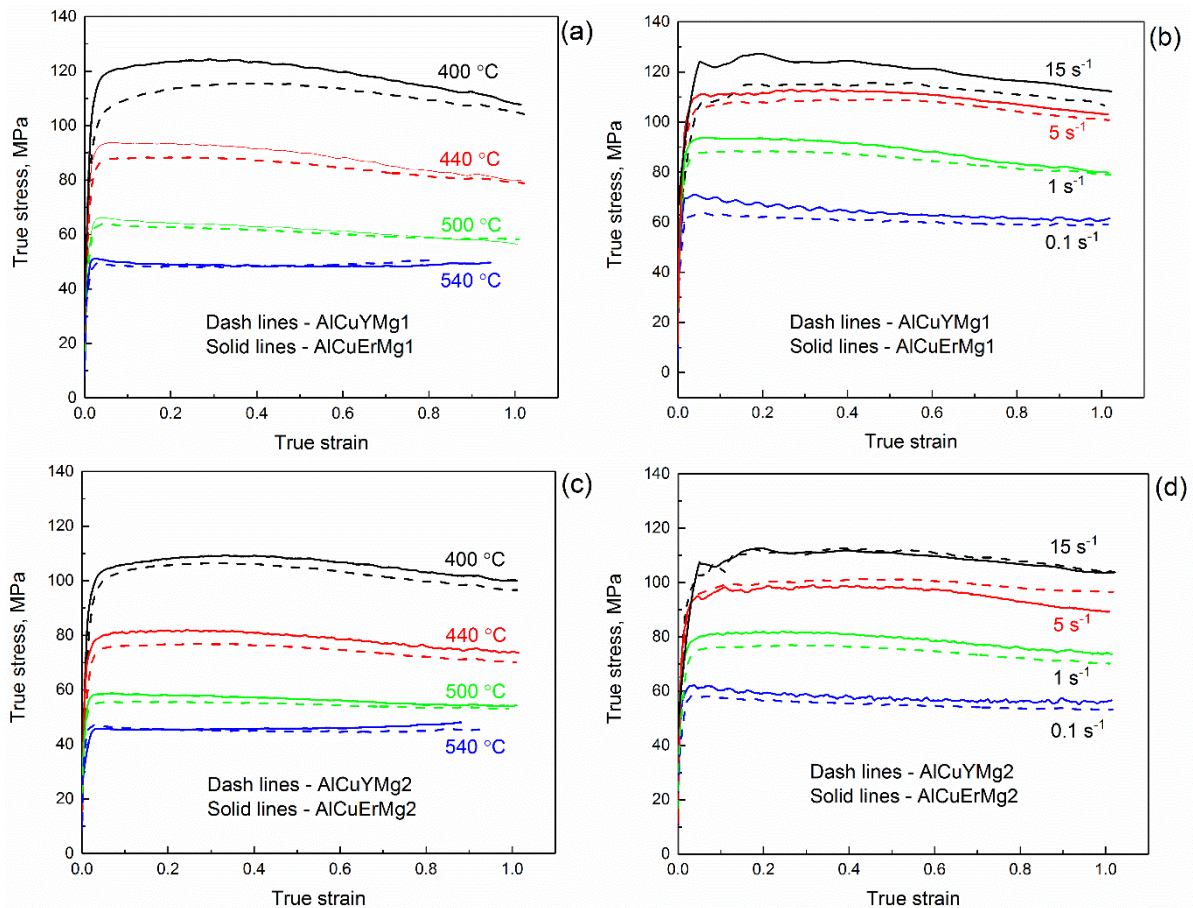


Figure 2. Typical true stress–true strain curves for the investigated alloys deformed at a strain rate of 1 s^{-1} (a,c) and at a temperature of $440 \text{ }^\circ\text{C}$ (b,d).

The elevated volume fraction of the intermetallic particles in the first group of the alloys led to an increase in the stress at all modes of deformation in comparison with the alloys containing lower particles. The particles are obstacles for the dislocation movement and do not provide the conditions for the particle stimulated nucleation due to high concentrations of the Mn and Zr. The stress level was slightly higher for the alloy with elevated Cu contents alloyed by Er (AlCuErMg1) in comparison with the Y-containing alloy (AlCuYMg1).

The quantitative analysis of the deformation behavior was carried out by constructing the Zener–Hollomon parameter-based constitutive model. The experimental values of the true stress at different strain rates ($\dot{\epsilon}$) and temperatures (T) at a strain of 0.8 were used for the building hyperbolic sine law model [36]:

$$Z = A_{\text{HS}}[\sinh(\alpha\sigma)]^{n_{\text{HS}}} \quad (1)$$

where Z is the Zener–Hollomon parameter [37]:

$$Z = \dot{\epsilon} e^{\frac{Q_{HS}}{RT}} \quad (2)$$

where A_{HS} , n_{HS} , and α are the experimentally determined parameters; Q_{HS} is the effective activation energy of hot deformation, J/mol; and R is the universal gas constant (8.314 J/mol·K).

However, the description of special cases of the constitutive models is required to determine the α parameter's value. The power-law form of the constitutive model is applicable for low stresses:

$$Z = A_P \sigma^{n_P} \quad (3)$$

The exponential form is usually used for elevated stresses:

$$Z = A_E e^{\beta \sigma} \quad (4)$$

where A_P , n_P , A_E , and β are the experimentally determined parameters.

The parameter α may be approximately determined as:

$$\alpha \approx \frac{\beta}{n_P} \quad (5)$$

The values of the constants in Equations (1) and (2) are shown in Table 3. The effective activation energy has a value in the range of 171–204 kJ/mol, which corresponds to the values obtained for the other aluminum alloys with a high content of intermetallic particles (e.g., 187 kJ/mol for the Al-4Ni-5.5Mg alloy [29] and 222 kJ/mol for the Al-10Sr master alloy). The effective activation energy Q_{HS} had a higher value for the alloys with Er than with Y for both low-alloyed and high-alloyed materials. The particles of the Er-containing phase may have higher strength than the Y-containing phases. As a result, the energetic barrier for the hot deformation of the AlCuErMg1 and AlCuErMg2 alloys was higher than for the AlCuYMg1 and AlCuErMg2 alloys.

Table 3. The values of the Zener–Hollomon parameter-based models.

Alloy	A_{HS}, s^{-1}	n_{HS}	α	$Q_{HS}, kJ/mol$
AlCuYMg1	$1.95 \cdot 10^{13}$	5.34	0.013	190
AlCuErMg1	$2.03 \cdot 10^{14}$	5.37	0.013	204
AlCuYMg2	$1.17 \cdot 10^{12}$	5.10	0.013	171
AlCuErMg2	$7.35 \cdot 10^{13}$	5.58	0.014	199

The accuracy of the constructed constitutive model was quantified using the average absolute relative error (AARE) and Pearson's correlation coefficient (R), which are expressed as [38]:

$$AARE(\%) = \frac{100}{N} \sum_{i=1}^N \frac{|E_i - C_i|}{E_i} \quad (6)$$

$$R = \frac{\sum_{i=1}^N (E_i - \bar{E})(C_i - \bar{C})}{\sqrt{\sum_{i=1}^N (E_i - \bar{E})^2 \sum_{i=1}^N (C_i - \bar{C})^2}} \quad (7)$$

Here, E and C are experimental and calculated by the model stress, and \bar{E} and \bar{C} are the mean values. N is the number of experiments used for the model construction. As shown in Figure 3, the model's accuracy was high ($R = 0.995$ and $AARE = 3.1\%$).

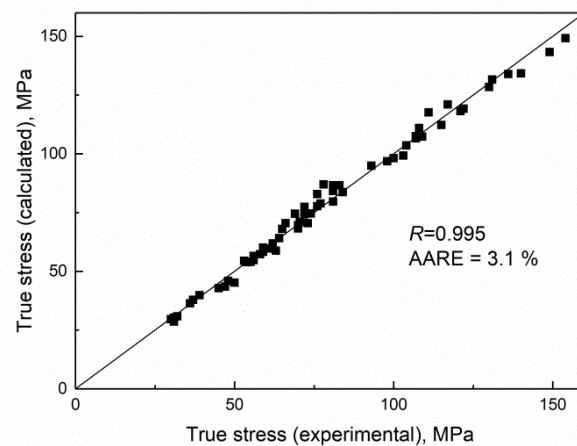


Figure 3. Comparison between the predicted and the experimental values of the flow stress.

3.3. Processing Maps

A hot processing map is a powerful tool to determine the optimal hot deformation technologies. This approach is based on the dynamic material model (DMM) suggested by Prasad and Gegel [39]. Processing maps may help determine the efficiency of power dissipation during forming and find unstable modes of deformation. The method linked the deformation medium mechanics with the evolution of the dissipative microstructure, which described the dynamic response of the microstructure during hot deformation. Such an approach was widely applied for the analysis of the hot deformation behavior of aluminum alloys. Optimal thermomechanical parameters were found using processing maps for Al4.5Zn4.5Mg1Cu0.12Zr(0.05–0.15)Sc [40], AA7020 [41], 6A02 [42], and 6063 [43] aluminum alloys.

Based on the dissipative structure theory, the total power required per unit volume of the material during hot deformation was described as:

$$P = \sigma \dot{\epsilon} = G + J = \int_0^{\dot{\epsilon}} \sigma d\dot{\epsilon} + \int_0^{\sigma} \dot{\epsilon} d\sigma \quad (8)$$

where P is the power dissipated during hot deformation; J is the power consumed by the evolution of the microstructure such as recrystallization, recovery, and phase transformation. Unfortunately, the integration of the stress–strain rate dependence in the form of hyperbolic sine law is impossible in the non-numeric form. This is the reason why the power-law is applied for the construction of processing maps:

$$\sigma = K \dot{\epsilon}^m \quad (9)$$

where K is the material constant, and m is the strain rate sensitivity coefficient:

$$m = \frac{\partial \ln \sigma}{\partial \ln \dot{\epsilon}} \quad (10)$$

J co-content can be written as

$$J = \int_0^{\sigma} \dot{\epsilon} d\sigma = \frac{m}{m+1} \sigma \dot{\epsilon} \quad (11)$$

The maximum possible dissipation was reached when $m = 1$, so J co-content obtains the maximum, which implies $J_{\max} = (\sigma \dot{\epsilon})/2 = P/2$.

The power dissipation efficiency η can be calculated by the equation as [41]:

$$\eta = \frac{J}{J_{\max}} = \frac{2m}{m+1} \quad (12)$$

The instability of the material during hot deformation is represented by the dimensionless parameter of ζ :

$$\zeta(\dot{\epsilon}) = \left[\frac{\partial \ln\left(\frac{m}{m+1}\right)}{\partial \ln \dot{\epsilon}} \right] + m < 0 \quad (13)$$

The processing maps for the investigated alloys are presented in Figure 4. Temperatures of 420–480 °C and strain rate higher than 5 s^{−1} were the most unwelcome deformation conditions for all the investigated alloys. This region on the processing maps is characterized by the minimum values of the power dissipation efficiency and the negative values of the flow instability. As a result, cracks on the surface of the samples appeared during deformation at 440 °C and 15 s^{−1} (Figure 5a). The deformation in conditions with a positive flow instability parameter and a higher value of power dissipation efficiency did not lead to the fracture of the sample (Figure 5b).

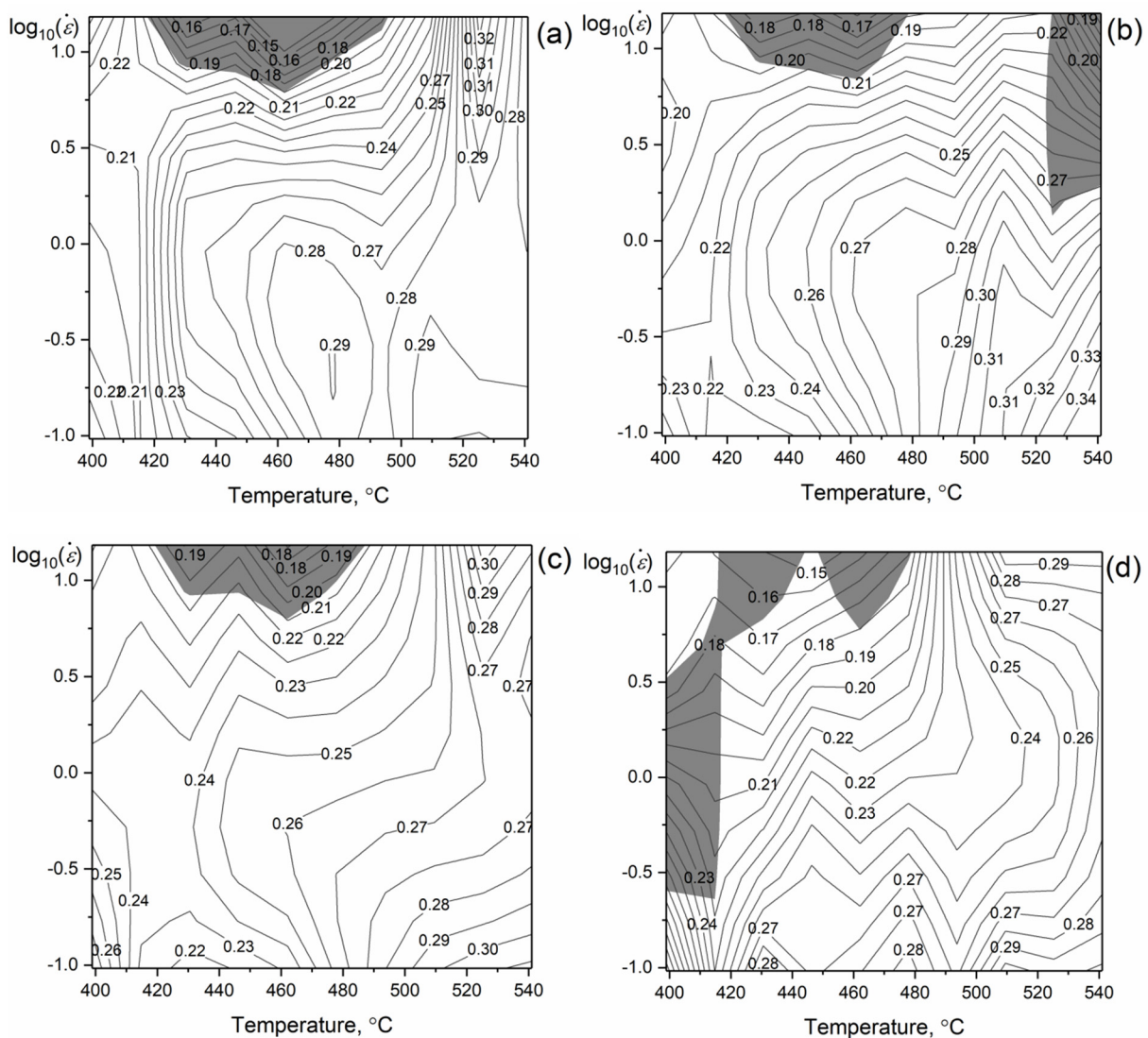


Figure 4. Processing maps of the investigated alloys: (a) AlCuYMg1, (b) AlCuErMg1, (c) AlCuYMg2, and (d) AlCuErMg2. Line contours are the values of the power dissipation efficiency (η), and the gray areas correspond to the negative values of the instability criteria.

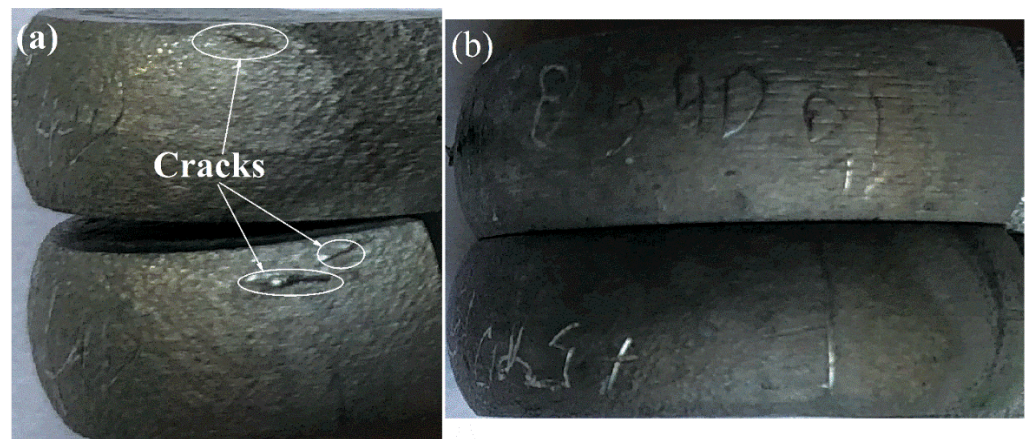


Figure 5. Image of the AlCuYMg1 and AlCuErMg1 alloys samples deformed at (a) 440 °C 15 s⁻¹ and (b) 540 °C 0.1 s⁻¹.

The microstructure after the deformation at different regions in processing maps is presented in Figure 6. According to the processing maps, no internal cracks were observed in the microstructure for the samples deformed at unfavorable regions. However, the low values of power dissipation efficiency are due to the fact that the microstructure is unrecrystallized after compression at 440 °C and a strain rate of 15 s⁻¹. The high concentration of the Mn and Zr prevented the growth of new grains. The increase in the deformation temperature to 540 °C led to dynamic recrystallization at a high strain rate of 15 s⁻¹. However, the deformation at a lower strain rate of 0.1 s⁻¹ did not provide conditions for dynamic recrystallization. The dynamic recovery fully neutralized stimulus for the appearance and the growth of new grains due to a long period of deformation and the high stacking fault energy of the (Al) solid solution [44,45].

The AlCuErMg1 and AlCuYMg1 alloys are more suitable as heat resistant cast alloys due to the high-volume fraction of the intermetallic particles, high strength at room and elevated temperatures [22], and the worst hot deformation behavior. The AlCuErMg2 and AlCuYMg2 alloys demonstrated a better hot deformation behavior, and the level of the room temperature strength of the wrought alloys was similar to the 2xxx alloys [23].

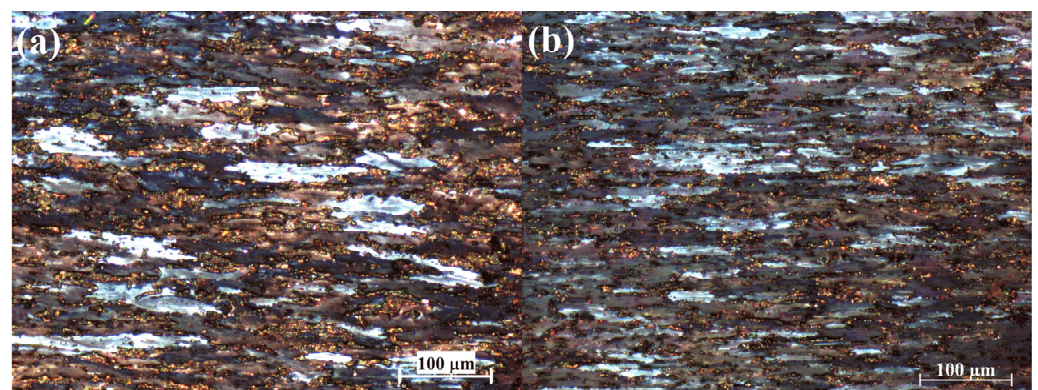


Figure 6. Cont.

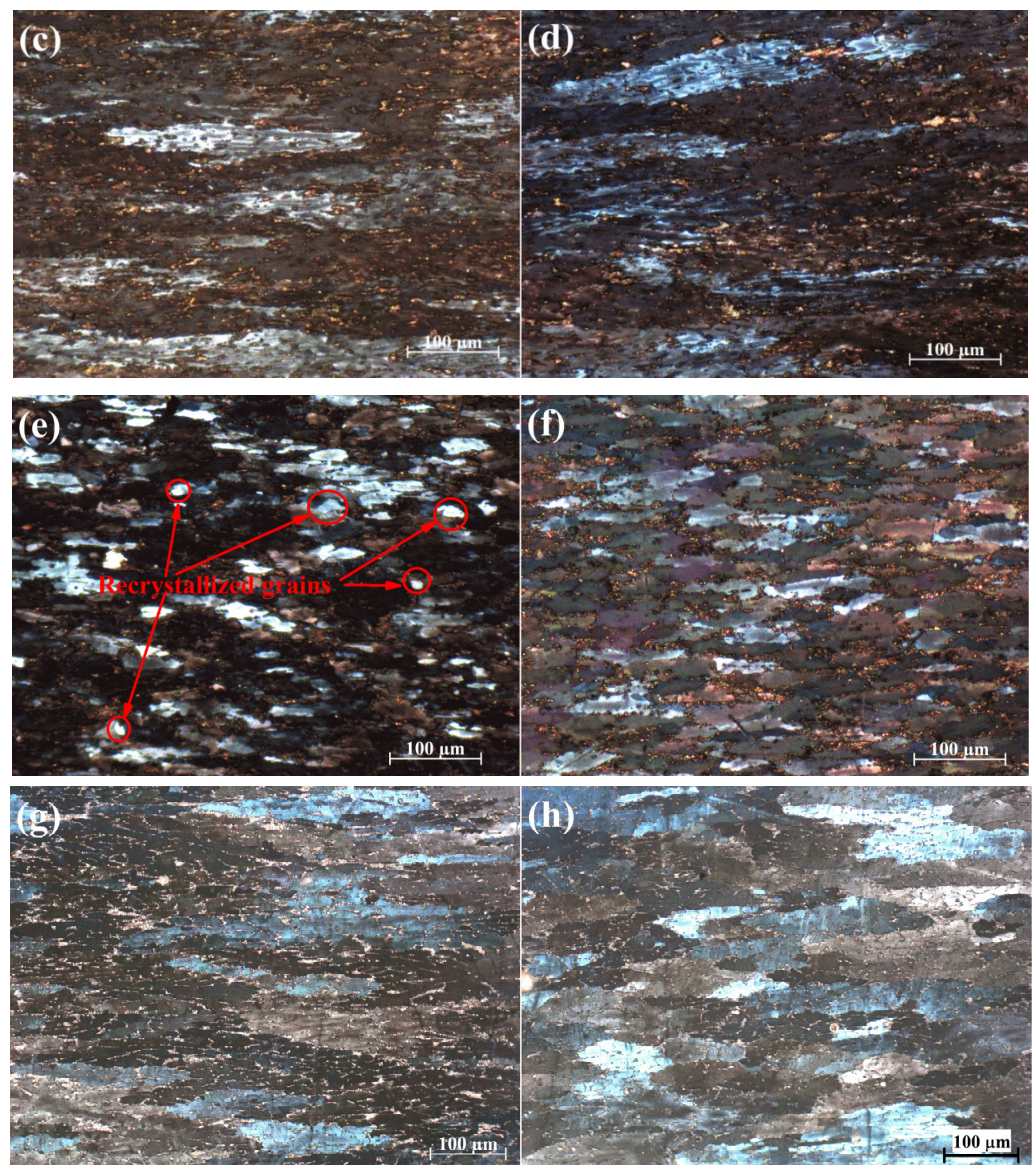


Figure 6. Grain microstructure of the investigated alloys AlCuYMg1 (a,e), AlCuErMg1 (b,f), AlCuYMg2 (c,g), and AlCuErMg2 (d,h) after compression at 440 °C and a strain rate of 15 s^{-1} (a–d); after compression at 540 °C and a strain rate of (e,g) 15 s^{-1} and (f,h) 0.1 s^{-1} .

4. Conclusions

- (1) The hot deformation behavior of four novel Al-Cu-Y(Er)-Mg-Mn-Zr alloys was investigated through compression tests in a temperature range of 400–540 °C and strain rates of 0.1–15 s^{-1} . A higher intermetallic particle content in the alloys led to an increase in flow stress at all the investigated temperatures and strain rates.
- (2) Hyperbolic sine law constitutive models of the Al-Cu-Y(Er)-Mg-Mn-Zr alloys' hot deformation behavior were constructed. Effective activation energy had a higher value in the alloys with Er than in those with Y.
- (3) The construction of the processing maps showed that a temperature range of 420–480 °C and strain rates higher than 5 s^{-1} were the most unfavorable region for hot deformation for all investigated alloys. The deformation at 440 °C and 15 s^{-1} led to cracks on the surface of the samples. However, internal cracks were not observed in the microstructure after deformation.

Author Contributions: Measurements: A.V.P., M.G.K., S.M.A.; Planning and supervision: A.V.P., R.Y.B.; Methodology: A.Y.C.; Experiments: A.Y.C., M.G.K., M.V.G.; Writing—original draft preparation: A.V.P. and A.Y.C.; Writing—review and editing: A.Y.C. and A.V.P.; Result analysis: M.G.K., S.M.A. and M.V.G. All authors have read and agreed to the published version of the manuscript.

Funding: This work was supported by the Russian Science Foundation (Project No. 19-79-10242).

Data Availability Statement: Not applicable.

Acknowledgments: The researcher S.M. Amer was funded by a partial scholarship from the Ministry of Higher Education of the Arab Republic of Egypt.

Conflicts of Interest: On behalf of all authors, the corresponding author states that there are no conflict of interest.

References

1. Snopiński, P.; Król, M.; Tański, T.; Pakuła, D.; Kríž, A. Effect of initial microstructure on hot deformation behavior of AlMg₅Si₂Mn alloy. *Mater. Charact.* **2021**, *177*, 111167. [\[CrossRef\]](#)
2. Xu, C.; He, H.; Xue, Z.; Li, L. A detailed investigation on the grain structure evolution of AA7005 aluminum alloy during hot deformation. *Mater. Charact.* **2021**, *171*, 110801. [\[CrossRef\]](#)
3. Bembalge, O.; Panigrahi, S. Hot deformation behavior and processing map development of cryorolled AA6063 alloy under compression and tension. *Int. J. Mech. Sci.* **2021**, *191*, 106100. [\[CrossRef\]](#)
4. Miao, J.; Sutton, S.; Luo, A.A. Microstructure and hot deformation behavior of a new aluminum–lithium–copper based AA2070 alloy. *Mater. Sci. Eng. A* **2020**, *777*, 139048. [\[CrossRef\]](#)
5. Wu, H.; Wen, S.; Huang, H.; Gao, K.; Wu, X.; Wang, W.; Nie, Z. Hot deformation behavior and processing map of a new type Al–Zn–Mg–Er–Zr alloy. *J. Alloy. Compd.* **2016**, *685*, 869–880. [\[CrossRef\]](#)
6. Scharifi, E.; Savaci, U.; Kavaklioglu, Z.; Weidig, U.; Turan, S.; Steinhoff, K. Effect of thermo-mechanical processing on quench-induced precipitates morphology and mechanical properties in high strength AA7075 aluminum alloy. *Mater. Charact.* **2021**, *174*, 111026. [\[CrossRef\]](#)
7. Jiang, Y.; Ding, H.; Cai, M.; Chen, Y.; Liu, Y.; Zhang, Y. Investigation into the hot forming–quenching integrated process with cold dies for high strength aluminum alloy. *Mater. Charact.* **2019**, *158*, 109967. [\[CrossRef\]](#)
8. Pozdniakov, A.; Barkov, R.Y. Microstructure and materials characterisation of the novel Al–Cu–Y alloy. *Mater. Sci. Technol.* **2018**, *34*, 1489–1496. [\[CrossRef\]](#)
9. Amer, S.; Barkov, R.Y.; Yakovtseva, O.A.; Pozdniakov, A.V. Comparative analysis of structure and properties of quasibinary Al–6.5 Cu–2.3 Y and Al–6Cu–4.05 Er alloys. *Phys. Met. Met.* **2020**, *121*, 476–482. [\[CrossRef\]](#)
10. Pozdniakov, A.; Barkov, R.Y.; Amer, S.; Levchenko, V.; Kotov, A.; Mikhaylovskaya, A. Microstructure, mechanical properties and superplasticity of the Al–Cu–Y–Zr alloy. *Mater. Sci. Eng. A* **2019**, *758*, 28–35. [\[CrossRef\]](#)
11. Amer, S.M.; Barkov, R.Y.; Pozdniakov, A.V. Effect of iron and silicon impurities on phase composition and mechanical properties of Al–6.3Cu–3.2Y alloy. *Phys. Met. Met.* **2020**, *121*, 1002–1007. [\[CrossRef\]](#)
12. Amer, S.M.; Barkov, R.Y.; Pozdniakov, A.V. Effect of Mn on the phase composition and properties of Al–Cu–Y–Zr alloy. *Phys. Met. Met.* **2020**, *121*, 1227–1232. [\[CrossRef\]](#)
13. Pozdniakov, A.V.; Barkov, R.; Sarsenbaev, Z.; Amer, S.; Prosviryakov, A.S. Evolution of microstructure and mechanical properties of a new Al–Cu–Er wrought alloy. *Phys. Met. Met.* **2019**, *120*, 614–619. [\[CrossRef\]](#)
14. Amer, S.M.; Barkov, R.Y.; Pozdniakov, A.V. Effect of impurities on the phase composition and properties of a wrought Al–6% Cu–4.05% Er alloy. *Phys. Met. Met.* **2020**, *121*, 495–499. [\[CrossRef\]](#)
15. Amer, S.; Barkov, R.Y.; Yakovtseva, O.A.; Loginova, I.S.; Pozdniakov, A.V. Effect of Zr on microstructure and mechanical properties of the Al–Cu–Er alloy. *Mater. Sci. Technol.* **2020**, *36*, 453–459. [\[CrossRef\]](#)
16. Amer, S.; Yakovtseva, O.; Loginova, I.; Medvedeva, S.; Prosviryakov, A.; Bazlov, A.; Barkov, R.; Pozdniakov, A. The phase composition and mechanical properties of the novel precipitation-strengthening Al–Cu–Er–Mn–Zr alloy. *Appl. Sci.* **2020**, *10*, 5345. [\[CrossRef\]](#)
17. Zhang, L.; Masset, P.J.; Tao, X.; Huang, G.; Luo, H.; Liu, L.; Jin, Z. Thermodynamic description of the Al–Cu–Y ternary system. *Calphad* **2011**, *35*, 574–579. [\[CrossRef\]](#)
18. Krachan, T.; Stel'makhovych, B.; Kuz'ma, Y. The Y–Cu–Al system. *J. Alloy. Compd.* **2003**, *349*, 134–139. [\[CrossRef\]](#)
19. Zhang, L.; Masset, P.J.; Cao, F.; Meng, F.; Liu, L.; Jin, Z. Phase relationships in the Al-rich region of the Al–Cu–Er system. *J. Alloy. Compd.* **2011**, *509*, 3822–3831. [\[CrossRef\]](#)
20. Zhang, L.; Liu, L.; Huang, G.; Qi, H.; Jia, B.; Jin, Z. Thermodynamic assessment of the Al–Cu–Er system. *Calphad* **2008**, *32*, 527–534. [\[CrossRef\]](#)
21. Belov, N.; Khvan, A. The ternary Al–Ce–Cu phase diagram in the aluminum-rich corner. *Acta Mater.* **2007**, *55*, 5473–5482. [\[CrossRef\]](#)
22. Amer, S.M.; Barkov, R.Y.; Prosviryakov, A.S.; Pozdniakov, A.V. Structure and properties of new heat-resistant cast alloys based on the Al–Cu–Y and Al–Cu–Er systems. *Phys. Met. Metallogr.* **2021**, *122*, 908–914. [\[CrossRef\]](#)

23. Amer, S.M.; Barkov, R.Y.; Prosviryakov, A.S.; Pozdniakov, A.V. Structure and properties of new wrought Al-Cu-Y and Al-Cu-Er based alloys. *Phys. Met. Metallogr.* **2021**, *121*, 913–920. [[CrossRef](#)]
24. Khomutov, M.G.; Bazlov, A.; Tsar'kov, A.A.; Churyumov, A. Simulation of flow stress of single-phase aluminum alloys of the Al-Mg, Al-Cu and Al-Zn systems in the process of hot deformation. *Met. Sci. Heat Treat.* **2013**, *55*, 393–396. [[CrossRef](#)]
25. Krallics, G.; Bézi, Z.; Bereczki, P. Hot deformation properties of 8006 aluminium alloy. *Procedia Manuf.* **2019**, *37*, 174–181. [[CrossRef](#)]
26. Wang, Q.; He, X.; Deng, Y.; Zhao, J.; Guo, X. Experimental study of grain structures evolution and constitutive model of isothermal deformed 2A14 aluminum alloy. *J. Mater. Res. Technol.* **2021**, *12*, 2348–2367. [[CrossRef](#)]
27. Hallberg, H.; Chamanfar, A.; Nanninga, N.E. A constitutive model for the flow stress behavior and microstructure evolution in aluminum alloys under hot working conditions—With application to AA6099. *Appl. Math. Model.* **2019**, *81*, 253–262. [[CrossRef](#)]
28. Rudnytskyj, A.; Simon, P.; Jech, M.; Gachot, C. Constitutive modelling of the 6061 aluminium alloy under hot rolling conditions and large strain ranges. *Mater. Des.* **2020**, *190*, 108568. [[CrossRef](#)]
29. Churyumov, A.Y.; Mikhaylovskaya, A.; Bazlov, A.I.; Tsarkov, A.A.; Kotov, A.D.; Aksenov, S.A. Influence of Al₃Ni crystallisation origin particles on hot deformation behaviour of aluminium based alloys. *Philos. Mag.* **2017**, *97*, 572–590. [[CrossRef](#)]
30. Wu, Y.; Liu, C.; Liao, H.; Jiang, J.; Ma, A. Joint effect of micro-sized Si particles and nano-sized dispersoids on the flow behavior and dynamic recrystallization of near-eutectic Al-Si based alloys during hot compression. *J. Alloy. Compd.* **2021**, *856*, 158072. [[CrossRef](#)]
31. Mikhaylovskaya, A.; Ghayoumabadi, M.E.; Mochugovskiy, A. Superplasticity and mechanical properties of Al-Mg-Si alloy doped with eutectic-forming Ni and Fe, and dispersoid-forming Sc and Zr elements. *Mater. Sci. Eng. A* **2021**, *817*, 141319. [[CrossRef](#)]
32. Zhang, Z.; Hu, J.; Teng, J.; Chen, J.; Zhao, G.; Jiang, F.; Fu, D.; Zhang, H. Hot compression and industrial extrusion characteristics of an as-cast Al-10Sr master alloy. *J. Manuf. Process.* **2021**, *61*, 481–491. [[CrossRef](#)]
33. Chankitmongk, S.; Eskin, D.G.; Limmaneevichitr, C. Constitutive behavior of an AA4032 piston alloy with Cu and Er additions upon high-temperature compressive deformation. *Met. Mater. Trans. A* **2019**, *51*, 467–481. [[CrossRef](#)]
34. Wan, Z.; Hu, L.; Sun, Y.; Wang, T.; Li, Z. Hot deformation behavior and processing workability of a Ni-based alloy. *J. Alloy. Compd.* **2018**, *769*, 367–375. [[CrossRef](#)]
35. Churyumov, A.Y.; Khomutov, M.G.; Tsar'kov, A.A.; Pozdnyakov, A.V.; Solonin, A.; Efimov, V.M.; Mukhanov, E.L. Study of the structure and mechanical properties of corrosion-resistant steel with a high concentration of boron at elevated temperatures. *Phys. Met. Met.* **2014**, *115*, 809–813. [[CrossRef](#)]
36. Sellars, C.; Mc Tegart, W. On the mechanism of hot deformation. *Acta Met.* **1966**, *14*, 1136–1138. [[CrossRef](#)]
37. Zener, C.; Hollomon, J.H. Effect of strain rate upon plastic flow of steel. *J. Appl. Phys.* **1944**, *15*, 22–32. [[CrossRef](#)]
38. Churyumov, A.; Khomutov, M.; Solonin, A.; Pozdniakov, A.; Churyumova, T.; Minyaylo, B. Hot deformation behaviour and fracture of 10CrMoWNB ferritic-martensitic steel. *Mater. Des.* **2015**, *74*, 44–54. [[CrossRef](#)]
39. Prasad, Y.V.R.K.; Gegel, H.L.; Doraivelu, S.M.; Malas, J.C.; Morgan, J.T.; Lark, K.A.; Barker, D.R. Modeling of dynamic material behavior in hot deformation: Forging of Ti-6242. *Met. Trans. A* **1984**, *15*, 1883–1892. [[CrossRef](#)]
40. Khomutov, M.G.; Pozdniakov, A.V.; Churyumov, A.Y.; Solonin, A.N.; Glavatskikh, M.V.; Barkov, R.Y. Flow stress modelling and 3D processing maps of scandium contents. *Appl. Sci.* **2021**, *11*, 4587. [[CrossRef](#)]
41. Ke, B.; Ye, L.; Tang, J.; Zhang, Y.; Liu, S.; Lin, H.; Dong, Y.; Liu, X. Hot deformation behavior and 3D processing maps of AA7020 aluminum alloy. *J. Alloy. Compd.* **2020**, *845*, 156113. [[CrossRef](#)]
42. Sun, Y.; Cao, Z.; Wan, Z.; Hu, L.; Ye, W.; Li, N.; Fan, C. 3D processing map and hot deformation behavior of 6A02 aluminum alloy. *J. Alloy. Compd.* **2018**, *742*, 356–368. [[CrossRef](#)]
43. Wu, R.; Liu, Y.; Geng, C.; Lin, Q.; Xiao, Y.; Xu, J.; Kang, W. Study on hot deformation behavior and intrinsic workability of 6063 aluminum alloys using 3D processing map. *J. Alloy. Compd.* **2017**, *713*, 212–221. [[CrossRef](#)]
44. Schulthess, T.; Turchi, P.; Gonis, A.; Nieh, T.-G. Systematic study of stacking fault energies of random Al-based alloys. *Acta Mater.* **1998**, *46*, 2215–2221. [[CrossRef](#)]
45. Zolotarevsky, N.; Solonin, A.; Churyumov, A.; Zolotarevsky, V. Study of work hardening of quenched and naturally aged Al-Mg and Al-Cu alloys. *Mater. Sci. Eng. A* **2009**, *502*, 111–117. [[CrossRef](#)]